This is a preprint, the final version is subject to change, of the American Mineralogist (MSA)
Cite as Authors (Year) Title. American Mineralogist, in press.
DOI: https://doi.org/10.2138/am-2020-7194

Revision 3

Texture and geochemistry of multi-stage hydrothermal scheelite in the Tongshankou porphyry-skarn Cu-Mo (-W) deposit, eastern China: implications for ore-forming process and fluid metasomatism

Jinsheng Han[a], Huayong Chen[a,] *, Wei Hong[b], Pete Hollings[c], Gaobin Chu[a], Le Zhang[d], Siquan Sun[e]

a. *Key Laboratory of Mineralogy and Metallogeny, Guangzhou Institute of Geochemistry, Chinese Academy of Sciences, Guangzhou 510640, China*

b. *ARC Centre of Excellence in Ore Deposits (CODES), University of Tasmania, Private Bag 79, Hobart 7001, Australia*

c. *Department of Geology, Lakehead University, 955 Oliver Road, Thunder Bay, Ontario P7B 5E1, Canada*

d. *State Key Laboratory of Isotope Geochemistry, Guangzhou Institute of Geochemistry, Chinese Academy of Sciences, Guangzhou 510640, China*

e. *Wuhan Institute of Geology and Mineral Resources, Wuhan 430205, China*

*Corresponding Author: Huayong Chen

Key Laboratory of Mineralogy and Metallogeny, Guangzhou Institute of Geochemistry, Chinese Academy of Sciences, Guangzhou 510640, China

Tel: +86-13926101976

Email: huayongchen@gig.ac.cn

Abstract

This is a preprint, the final version is subject to change, of the American Mineralogist (MSA)
Cite as Authors (Year) Title. American Mineralogist, in press.
DOI: https://doi.org/10.2138/am-2020-7194

Scheelite from the Tongshankou porphyry-skarn Cu-Mo (-W) deposit occur mainly as disseminated grains in the altered granodiorite porphyries at depth (Sch A), in the skarn coeval with retrograde alteration (Sch B) and in distal quartz veins crosscutting marbles (Sch C). Cathodoluminescence (CL) responses within a single Sch A grain reveal two subtypes: CL-clear Sch A-I and CL-turbid, densely veined Sch A-II. The CL contrast, coupled with geochemical data, suggest Sch A-I was metasomatized to form Sch A-II. CL images reveal that Sch A-I, Sch B and Sch C are all homogenous, with blue luminescence and are depleted in heavy rare earth elements (HREE), indicating a primary origin. However, Sch A-II is characterized by higher contents of light REE and heavy REE as well as higher Sr isotopes (0.7080–0.7100) than the primary scheelite (< 0.7080). These differences indicate that Sch A-II formed through dissolution-reprecipitation. The Sr isotopes of the primary scheelite (0.7073–0.7078) are generally consistent with those of the mineralized granodiorite porphyries (0.7061–0.7063) and mafic enclaves (0.7058–0.7073). The granodiorite porphyries contain low tungsten contents (3–11 ppm), whereas high tungsten contents were detected in mafic enclaves (48–75 ppm). The coexistence of mafic enclaves and tungsten mineralization at depth, and their consistent Sr isotopes indicate that the interaction of mafic enclaves and exsolved magmatic fluids from the granodiorite porphyries may have played an important role in the extraction of tungsten from the mafic enclaves and formation of scheelite mineralization. Our work shows that scheelite geochemistry can be used to trace the mineralizing conditions but the compositions may be significantly modified during ore-forming process. Thus,

detailed textural relationships should be investigated before using scheelite geochemistry to constrain the hydrothermal fluids and ore genesis.

Keywords: scheelite, metasomatic alteration, dissolution-reprecipitation, mineral textures, mineral geochemistry

Introduction

The elemental geochemistry of minerals has been widely used as tracers of magmatic processes (e.g. Lipin and McKay, 1989; Ware et al., 2018). However, in hydrothermal systems, it is more challenging as the element distribution in hydrothermal minerals could be modified during formation, transportation or precipitation as well as during subsequent hydrothermal events (Uspensky et al., 1998; Smith et al., 2004; Gaspar et al., 2008). During those processes, some trace elements will be remobilized and some new mineral phases could be generated (Putnis, 2002, 2009; Geisler et al., 2007; Deditius et al., 2018). For example, such modification of magnetite, apatite, sulfides and zircon in hydrothermal systems have been recently reported (Geisler et al., 2007; Hu et al., 2014; Zhao et al., 2014; Zeng et al., 2016), which caution the use of elemental geochemistry in deciphering the hydrothermal ore genesis.

Scheelite and wolframite are two main tungsten minerals (Wood and Samson, 2000). Scheelite ($CaWO_4$) is well developed in porphyry and skarn related polymetallic deposits and is often coeval with other ore minerals such as chalcopyrite and cassiterite (Nobel et al., 1984; Brugger et al., 2000; Song et al., 2014; Fu et al., 2017). Scheelite is also a common accessory hydrothermal mineral that often coexists

with gold in quartz vein-hosted gold deposits (Darbyshire et al., 1996; Ghaderi et al., 1999; Brugger et al., 2002). Scheelite has a simple tetrahedral $[WO_4]^{2-}$ and dodecahedral $[CaO_8]^{14-}$ crystal structure and can host high contents of rare earth elements (REEs), Sr, and Pb through substitution of Ca^{2+} in the mineral lattice (Uspensky et al., 1998; Ghaderi et al., 1999; Dostal et al., 2009). Rubidium/Sr ratios in scheelite are typically very low (approximately zero) because of its inability to incorporate Rb into its lattice (Bell et al., 1989; Darbyshire et al., 1996; Chugaev et al., 2010). This means $^{87}Sr/^{86}Sr$ changes little over time, so as long as the system remain closed the measured isotope ratio can directly reflect the Sr isotopic characteristics of the fluids from which the scheelite crystallized. This important feature, together with the high contents of REEs and other trace elements make scheelite a powerful tool for investigating fluids associated with hydrothermal mineralization (Ghaderi et al., 1999; Song et al., 2014; Sun et al., 2017; Plotinskaya et al., 2018). However, scheelite can be hydrothermally modified, resulting in inhomogeneous REE patterns across an individual grain, as demonstrated by distinct internal structures under CL (e.g., Archaean Mt. Charlotte Lode Au deposit; Brugger et al., 2002). Thus, without detailed textural studies, the geochemistry of scheelite may provide misleading information.

The Middle-Lower Yangtze River metallogenic belt (MLYRB) has long been considered an important porphyry-skarn Fe and Fe-Cu mineralization province (Fig. 1a; Ling et al. 2009; Li et al. 2010; Zhou et al. 2015). A number of W-Mo deposits have been discovered in recent years (Zhu et al., 2014; Lei et al., 2018), including the

Tongshankou porphyry-skarn deposit located in the Edong district of the MLYRB. Tongshankou is a large Cu-Mo-(W) polymetallic deposit that contains a resource of 0.5 Mt Cu, 2000 t Mo and 12,000 t WO_3 (Fig. 1b; Li et al., 2008). The origin and paragenesis of the scheelite mineralization remains enigmatic. We present a combination of cathodoluminescence images, in situ major and trace elements and Sr isotopes of well-characterized scheelite grains in order to 1) investigate the formation mechanism of variable generations of scheelite grains in a single deposit, 2) decipher the evolution of the ore-forming fluids and the source for the tungsten.

Regional and deposit geology

The MLYRB, extending from Echeng in the west to Zhenjiang in the east, contains more than 200 porphyry, skarn and stratiform Cu-Au-Mo-Fe deposits (Lai et al. 2007; Ling et al. 2009; Zhou et al. 2015; Fig. 1a). These deposits are distributed in seven ore clusters including Edong, Jiurui, Anqing-Guichi, Luzong, Tongling, Ningwu, and Ningzhen (Fig. 1a; Lai et al. 2007; Xie et al. 2012). In the Edong ore cluster, more than 50 porphyry-skarn and skarn Cu-Fe-Au-Mo deposits are hosted in extensive Cambrian to Middle Triassic marine carbonates, clastic and flysch sequences (> 6000 m in thickness; Fig. 1b; Xie et al. 2012, 2015, 2016; Xia et al. 2015), genetically associated with felsic to intermediate intrusions with ages ranging from 150 to 120 Ma (Fig. 1b; e.g., Li et al. 2009).

Recent deep drilling has identified scheelite mineralization in the Tongshankou porphyry-skarn system (Zhu et al., 2018). The deposit is closely associated with the granodiorite porphyries which commonly host microgranular enclaves whose

abundance generally increases with depth (Figs. 2, 3a; Wang et al. 2004; Li et al. 2008). The Tongshankou stocks were emplaced into the limestone and dolomitic limestone of the Lower Triassic Daye Formation at about 140 Ma via LA-ICP-MS zircon U-Pb dating, within error of Re-Os molybdenite ages (~143 Ma: Lv et al. 1992; Shu et al. 1992; Li et al. 2008).

Sampling and analytical methods

The scheelite samples (28N1-90: Sch A; 28N1-92: Sch B; 901-63: Sch C) were collected from drill holes B28NZK1 (28N1-90: -448.42 m; 28N1-92: -451.3 m) and B09EZK1 (901-63: -490.3 m). The calcite coexisting with Sch A in sample 28N1-90 was also chosen for in situ Sr isotope analysis. Polished sections of these samples were made for microscopic observations. Scheelite grains were separated and handpicked under a binocular microscope. The grains were mounted in epoxy and polished for further observation and analysis.

SEM and Cold Cathodoluminescence

SEM-CL images of scheelite were acquired to image the internal structure, using Carl Zeiss SIGMA 300 field emission scanning electron microscope, equipped with an Oxford X-MAX020 energy-dispersive spectroscopy (EDS) at the School of Earth Sciences and Engineering, Sun Yat-sen University (SYSU). The applied acceleration voltage and current were 15 kV and ca. 25 nA, respectively. We also used a cold cathode generator CL8200 MK5, with a Quanta FEG 650 from FEI Corporation operating at about 10 keV and 250 mA, with imagery taken using a 3 s exposure time on thin sections at China University of Geosciences (Wuhan). The samples were

133 photographed at 298 K. The former technique could reflect the internal texture
134 whereas the later one could be used to reflect the composition of scheelite.

135 ***Electron probe analytical method***

136 Major element compositions of scheelite grains were obtained at the Shandong
137 Analysis Center of the China Metallurgical Geology Bureau using a JEOL JXA-8230
138 electron microprobe at an accelerating voltage of 20 kV with a 20 nA beam current, 1
139 um beam diameter for all elements. Natural minerals and synthetic oxides were used
140 as standards (albite for Na, olivine for Mg, Cr-diopside for Ca, magnetite for Fe,
141 rhodonite for Mn, rutile for Ti, orthoclase for K, Cr2O3 for Cr, metal Cu for Cu,
142 ZnWO4 for W, molybdenite for Mo, and metal Sn for Sn). Peak and background
143 counting times were 20 and 10 s for Ca, W, 20 to 40 s for the other elements. All data
144 were corrected with the ZAF procedures. The detection limit is 0.015% for most of
145 the elements and the precision is commonly better than 1.5%.

146 ***LA-ICP-MS measurement***

147 Trace element concentrations in scheelite were measured by Laser Ablation
148 Inductively-Coupled Plasma Mass Spectrometry (LA-ICP-MS) on polished thick
149 sections at the In situ Mineral Geochemistry Lab, Ore Deposit and Exploration Centre
150 (ODEC), Hefei University of Technology, China. The analyses were carried out on an
151 Agilent 7900 Quadrupole ICP-MS coupled to a Photon Machines Analyte HE 193-nm
152 ArF Excimer Laser Ablation system. Each analysis was performed using a uniform
153 spot size diameter of 44 um at 8 Hz with energy of ~4 J/cm^2 for 40s after measuring
154 the gas blank for 20s. Standard reference materials BCR-2G and NIST 610 were used

as external standards to plot the calibration curve. The preferred concentrations for the USGS reference glasses are from the GeoReM database (http://georem.mpch-mainz.gwdg.de/). Standard reference materials were run after each 10-15 unknowns with detection limits calculated for each element in each spot analysis.

The off-line data processing was performed using the program ICPMSDataCal (Liu et al., 2008). Internal element standard calibration was used when possible for mineral trace elements analysis. Although scheelite is an anhydrous mineral and there is no need to consider the H_2O and volatiles during the analysis, it is zoned in Ca, W, and Mo and hard to be analyzed with the same volume by both electron microprobe and LA-ICP-MS, which means we cannot use those elements as major-element internal standards. Shen et al. (2018) achieved satisfactory accuracy for major and trace element data in anhydrous minerals using multiple reference materials without applying internal standardization. The analytical precisions for most measured elements are better than 8% and the results agree with their reference values within +/-10%.

In situ Sr isotopes

In situ Sr isotope analyses were performed at the State Key Laboratory of Isotope Geochemistry, Guangzhou Institute of Geochemistry, Chinese Academy of Sciences (GIG-CAS) using a Neptune Plus MC-ICP-MS (Thermo Scientific), coupled with a RESOlution M-50 193 nm laser ablation system. Detailed methods are referred to Zhang et al. (2014). The operating conditions were as follows: beam diameter,

112–155μm; repetition rate, 6 Hz; energy density, ~4 J cm^{-2}. Correction for ^{87}Rb used measured the natural $^{85}Rb/^{87}Rb$ with a value of 2.593 (Catanzaro et al., 1966). The mass bias of $^{87}Sr/^{86}Sr$ was normalized to $^{86}Sr/^{88}Sr = 0.1194$ with an exponential law. The detailed data reduction procedure was reported in Zhang et al. (2018).

Results

Scheelite distribution and classification

Hydrothermal alteration and mineralization of the Tongshankou porphyry-skarn deposit have been described in detail by Han et al. (2018), with porphyry mineralization consisting of potassic alteration, phyllic alteration and carbonate stage and skarn-type alteration and mineralization consisting of the early skarn stage, late skarn stage, oxide stage, quartz-sulfide stage and late vein stage.

Scheelite was only observed at depth and occurs mainly in areas of skarn alteration (Fig. 2). They commonly occur as disseminations in the altered granodiorite porphyries (Sch A; Figs. 3b, c), in the skarn coeval with retrograde alteration (Sch B; Figs. 3d, e) and in distal quartz veins (Sch C) crosscutting marble (Figs. 3f, g). The three types of scheelite grains have distinct mineral assemblages, that are: 1) Sch A coexisting with calcite and chalcopyrite (Figs. 4a, c), 2) Sch B occurring with sericite and chalcopyrite (Fig. 4e) and 3) Sch C occurring with quartz in distal quartz veins (Fig. 4g).

Cathodoluminescence (CL) imaging

Sch A shows complex CL textures, consisting of turbid Sch A-II and clear Sch A-I (Figs. 4b, d, 5b). Sch A-I is typically much clearer than type A-II (Figs. 4b, d).

The blue luminescence of Sch A-I is vaguely zoned. The Sch-II shows lighter blue luminescence and a concentration of blue-white luminescent veins. Many veins are seen to traverse Sch A-I. In addition, Sch A-I shows blue luminescence whereas Sch A-II shows light blue luminescence, the latter also crosscuts the rims of Sch A-I (Figs. 4b, d). SEM-CL also reveals complex textures of Sch A, as demonstrated by CL-dark gray and CL-bright gray scheelite in individual grain (Fig. 5b). Meanwhile, many pores were developed in CL-dark gray Sch A, where mica was observed (Fig. 5b). Sch B and Sch C show blue luminescence with relatively homogenous CL intensity (Figs. 4f, h), consistent with the generally CL-bright gray color under SEM-CL (Figs. 5d, f).

Major and trace element geochemistry

Major element data for scheelite are presented in Supplementary Table 1. These scheelite grains have 75.4–81.5 % WO_3, 18.8–19.7 % CaO and 0–1.7 % MoO_3 with only subtle differences among the four types of scheelite grains (Sch A-I, A-II, B and C). The scheelite grains all have minor concentrations of Na_2O, MgO, MnO, FeO, TiO_2, K_2O, Cr_2O_3, SnO_2, CuO.

A total of 52 trace elements were measured by LA-ICP-MS on the scheelite from the Tongshankou deposit. Representative results are presented in Supplementary Table 2. The scheelite grains have variable abundances of Sr, Nb, Na and Mo, and the abundances of other trace elements are either minor or close to the detection limit. Although all the scheelite types are enriched in light rare earth elements (LREE) relative to heavy REE (HREE; Figs. 5a, c, e), each type is characterized by distinct

distribution patterns. Analyses of Sch A-I show strong negative chondrite-normalied Eu anomalies (Fig. 5a). The Sch A-II grains have positive Eu anomalies and have the highest total REE contents of all samples analyzed (Fig. 5a). Rare-earth patterns of Sch B and C have positive and negative Eu anomalies, respectively (Fig. 5c, e). The Eu anomalies of the four types of scheelite do not show obvious correlation with Sr and Mo contents (Fig. 6).

In situ Sr isotopes of scheelite and calcite

In situ Sr isotopes of scheelite and calcite that coexist with Sch A are presented in Supplementary Table 3. The measured $^{87}Sr/^{86}Sr$ ratios of scheelite range from 0.7073–0.7079 for Sch A-I, 0.7080–0.7100 for Sch A-II, 0.7064–0.7068 for Sch B and 0.7076–0.7078 for Sch C (Fig. 7). The calcite have a wide $^{87}Sr/^{86}Sr$ ratios ranging from 0.7072 to 0.7085 (Fig. 7).

Discussion

Dissolution and reprecipitation of scheelite

Our studies show that cold-cathode and SEM-CL can highlight cryptic textures in scheelite that cannot be revealed via transmitted or reflected light imaging (Figs. 4a-d). The scheelite in the Tongshankou deposit generally show homogeneous blue luminescence (Fig. 4). However, Sch A shows complex CL textures as reflected by light-blue luminescent Sch A-II with cracks and vaguely zoned deep-blue luminescent Sch A-I being distributed in a single grain (Figs. 4b, d). SEM-CL image also reveals complex textures consisting of both dark- and bright-gray zones in an individual grain (Fig. 5b).

The pores in Sch A-II indicate that dissolution has occurred and that there would have been a small loss of material liberated into the ambient fluids (Fig. 5b). As crystal defects can produce different CL responses due to specific physical and chemical conditions under which the hydrothermal mineral grew (Rusk and Reed, 2002; Rusk et al., 2008), the CL-dark gray and CL-bright gray zones in an individual grain represent different generations of scheelite in equilibrium with fluids of different physical and chemical conditions (Figs. 5b; Rusk and Reed, 2002).

A close spatial relationship and sharp reaction fronts observed between Sch A-I and Sch A-II, without changing the shape of the primary crystals, indicate a replacement process through the almost coeval occurrence of dissolution and reprecipitation (Putnis, 2009; Fig. 5b). Sch A-II is sometimes surrounded by the parental Sch A-I, a feature that can be explained by cracks in the inner part of Sch A (Figs. 4b, d), which allowed the percolation of fluids through the primary mineral phase and thus, dissolved Sch A-I and precipitate Sch A-II in the core. During this process, compositional exchange between the fluids and Sch A-I occurred, resulting in Sch A-II having a different composition compared to Sch A-I in terms of REE patterns, Eu anomalies, Mo concentrations and Sr isotopes (Figs. 5a, 6b, 7). Besides, Sch A-I may differ to Sch A-II on molar volume and solubility, the combination of which would have led to the development of pores in Sch A-II, which is the common feature of the product phase (Putnis, 2009).

The sources of the tungsten and ore-forming fluids

All of three types of scheelite coexist with hydrothermal chalcopyrite (Figs. 3f, g,

4), indicating they were generated from hydrothermal fluids, not directly from magma (Han et al., 2018). According to the above discussion, Sch A-I should represent primary hydrothermal scheelite mineralization in the skarn system of the Tongshankou deposit. The relatively homogeneous appearance and the similar blue luminescence (Figs. 4f, h, 5d, f) indicate that the Sch B and C have not been modified by later hydrothermal fluids, i.e., they can represent their primary geochemical characteristics. Previous studies have shown that the skarn Cu-Mo mineralization was closely related to the granodiorite porphyry widely distributed at Tongshankou (e.g. Li et al., 2008). However, the newly identified scheelite mineralization only occurred at depths > 350 m of the drillholes, indicating the source of tungsten should not come only or directly from the granodiorite porphyries, which is supported by their low tungsten contents ranging 3–11 ppm (Supplementary Table 4). In contrast, mafic enclaves commonly occurring in granodiorite porphyries at depth have high tungsten contents ranging 48–75 ppm (Supplementary Table 4), indicating that the mafic enclaves may contribute to the source of tungsten. No separate tungsten minerals were identified in the mafic enclaves (Supplementary Fig. 1). Compared to the granodiorite porphyry, the mafic enclaves host more biotite (Supplementary Fig. 1). Biotite from the granodiorite porphyry have tungsten concentrations ranging from 0.12 to 1.43 ppm whereas those from the mafic enclaves have tungsten concentrations ranging from 25.56 ppm to 279 ppm (Supplementary Table 5). The higher tungsten concentrations in the biotite from the mafic enclaves let us to propose that at least part of the tungsten may come from the mafic enclaves.

Fluid-host rock interaction can affect the Sr isotopic composition of fluids (Lv et al. 1992; Shu et al. 1992; Li et al. 2008; Scanlan et al., 2018). Some scheelite in magmatic systems such as the Shimensi W-Cu-Mo deposit in South China have low Sr concentrations (200–1000 ppm). In that system, fluid-rock interaction with Sr-rich metasedimentary host rocks led to widely variable $^{87}Sr/^{86}Sr$ ratios in scheelite (0.7230–0.7657; Sun et al., 2017). At Tongshankou, scheelite mineralization resides mainly in the skarn and coexists with chalcopyrite, implying the scheelite should be hydrothermal minerals in the skarn system. Its formation involved the interaction from the exsolved fluids from the granodiorite porphyry and carbonates. The host rocks are mainly marine carbonates which typically have $(^{87}Sr/^{86}Sr)_i$ values lower than 0.7060 (Xu and Jiang, 2017). The measured $^{87}Sr/^{86}Sr$ ratios for Sch A-I and Sch C have overlapping ranges of 0.7073–0.7079, 0.7076–0.7078, respectively, whereas the ratios for Sch B range 0.7064–0.7068. The lower $^{87}Sr/^{86}Sr$ in Sch B suggests greater involvement of carbonates in the formation of this group of scheelites, which is consistent with Fig. 3d, e.

Meanwhile, all these ratios are comparable to the Sr isotopic composition of the porphyry granodiorites and mafic enclaves (Fig. 7; porphyry granodiorites: 0.7061–0.7063; mafic enclaves: 0.7058–0.7073; Li et al., 2008). The similar Sr isotopes, high tungsten contents in the mafic enclaves, the occurrence of scheelite at depth and the coexistence of scheelite with chalcopyrite in skarn all imply that the primary ore-forming fluids for the scheelite mineralization were likely to have resulted from the interaction between mafic enclaves and exsolved

magmatic-hydrothermal fluids from the granodiorite porphyries.

REE substitution mechanism in primary scheelite

Three main coupled substitution mechanisms that can introduce REE into the scheelties are: 1) $2Ca^{2+} = REE^{3+} + Na^{+}$; 2) $Ca^{2+} + W^{6+} = REE^{3+} + Nb^{5+}$; 3) $3Ca^{2+} = 2REE^{3+} + \square_{Ca}$, where $\square_{Ca}$ represents a Ca site vacancy (Nassau and Loiacono, 1963; Burt, 1989; Uspensky et al., 1998; Ghaderi et al., 1999). Different substitution mechanisms will result in distinct REE patterns of scheelite (e.g. Ghaderi et al., 1999).

The extremely low contents of Nb compared to the ΣREE and the absence of correlation between the ΣREE and Nb preclude Nb-dominated substitution in the Tongshankou scheelite (Fig. 8a). Given the linear trend along the 1:1 line between Na and total REE in Sch C, it is most probable that Na-substitution occurred in Sch C (Fig. 8b). However, Ghaderi et al. (1999) stated that Na-substitution in scheelite will result in hump-like REE patterns, which are not observed in Sch C. Sch C is characterized by higher Sr concentration than the other scheelite (Fig. 6a), indicating the involvement of Sr during the REE substitution. We speculate that involvement of Sr^{2+} was responsible for the absence of hump-like REE pattern in Sch C. As to the other types of scheelite, no correlation exists between Na and ΣREE + Y – Eu, excluding the involvement of Na-substitution mechanism (Fig. 8b).

Calcium site vacancies can provide the charge compensation in scheelite and will generate REE patterns inherited from the ore-forming fluids (Ghaderi et al., 1999; Song et al., 2014). The Tongshankou scheelite are characterised by depletion of HREE except for the Sch A-II which resulted from modification of Sch A-I (Figs. 5a,

c, e). Based on our detailed observations, the occurrence of scheelite (Figs. 4a, c, e, g) should be later than that of garnet occurring in early skarn alteration. The original garnets at Tongshankou also show HREE-depletion (LA-ICP-MS results, unpublished data), suggesting the initial ore-forming fluids were also depleted in HREE. Therefore, the HREE-depleted pattern of Sch A-I and B were likely inherited from the initial ore-forming fluids, indicating that $\square_{Ca}$-substitution is the most probable mechanism. In this scenario, the partitioning coefficients of REEs between scheelite and the melt or solution are approximately identical and the REE patterns of Sch A-I and B could be used to trace the ore-forming fluids (Nassau and Loiacono, 1963).

Oxygen fugacity of the primary ore-forming fluids

Based on the above discussion, the REE patterns of Sch C has been disturbed by the Na substitution mechanism while those of Sch A-II reflect later involved fluids. The REE patterns of Sch A-I and B record the characteristics of ore-forming fluids. As Mo is a redox-sensitive element (Elbaz-Poulichet et al., 2005), we compare the Mo concentration with Eu/Eu* to determine whether Eu anomalies could reflect redox conditions of hydrothermal fluids. Sch A-I is characterised by Eu/Eu* < 1 and elevated Mo, whereas Sch B is characterized by Eu/Eu* > 1 and low Mo (Fig. 6b). This phenomenon suggests that changes in Eu anomalies in Sch A-I and B were related to redox conditions of hydrothermal fluids. The absence of obvious linear correlation between Eu anomalies and Mo concentration (Fig. 6b) perhaps indicates that Eu anomalies were not only related to the fO_2 of hydrothermal fluids but also affected by the fluid pH or different partition coefficients between Eu^{2+} and Eu^{3+}

(Ghaderi et al., 1999; Brugger et al., 2000, 2008).

Oxidized Mo (Mo^{6+}) will tend to enter scheelite by substituting for W^{6+} whereas reduced Mo (Mo^{4+}) will tend to precipitate as molybdenite (Ghaderi et al., 1999; Zhao et al., 2018). According to Mo compositions in each scheelite type (Fig. 6), negative Eu anomalies in Sch A-I may reflect more oxidizing conditions and positive Eu anomalies of Sch B formed from a more reduced fluid (Ghaderi et al., 1999; Brugger et al., 2000; Poulin et al., 2018; Zhao et al., 2018). This suggests that the scheelite-fluid partition coefficient of Eu^{2+} may be greater than that of Eu^{3+}. The decrease in Mo concentration from Sch A-I to Sch B may thereby reflect a progressive decrease in f_{O2} of hydrothermal fluids.

Metallogenic model

Combined with previous studies, the metallogenic model for the Tongshankou mineralization could be expressed as: magmatic-hydrothermal fluids exsolved from the granodiorite porphyries interacted with the carbonate host rocks and generated skarn alteration and copper ore bodies. At depth, the magmatic-hydrothermal fluids interacted with the tungsten-rich mafic enclaves, forming disseminated scheelite mineralization in the granodiorite porphyries (Sch A), in the contact between the carbonates and the granodiorite porphyries (Sch B), and along the cracks of the carbonates in the distal area (Sch C; Fig. 9a).

It is difficult to form Sch A-II with high REE concentrations without the incursion of a REE-rich external fluid (Fig. 5a). Commonly, calcites have low $(^{87}Sr/^{86}Sr)_i$ values (<0.7060; Xu and Jiang, 2017). The large distribution of $^{87}Sr/^{86}Sr$

ratios of the Tongshankou calcites, especially those high values similar to Sch A-II ratios (Fig. 7) may be due to the involvement of an external fluid with high initial Sr isotopes. The presence of mica in the pores of the Sch A-II also supports the presence of K^+ in the fluid (Fig. 5b). In summary, a later fluid, enriched in K and REE and with high $(^{87}Sr/^{86}Sr)_i$, attacked and modified Sch A-I grains, resulting in the textures and compositions observed in Sch A-II (Fig. 9b).

Implications

Cold and SEM-CL imaging of scheelite can reveal textures that are not seen under transmitted light, including those resultant from dissolution-reprecipitation processes. At Tongshankou, dissolution-reprecipitation yielded scheelite with strongly modified REE patterns and Sr isotopes without significantly modifying their morphology and appearance. Therefore, it is crucial to evaluate such processes according to the textures and geochemical characteristics before using scheelite as an indicator mineral when studying hydrothermal ore deposits.

This study also provides a good example of the use of scheelite textures and geochemistry to reveal the nature and source of ore-forming fluids. The scheelite-precipitating fluids were not depleted in Mo based on the coexistence of molybdenite and chalcopyrite (Han et al., 2018) and the coexistence of scheelite and chalcopyrite (Figs. 4a, c). The Mo contents in the scheelite reflect the fluid oxygen fugacity and together with the Eu anomalies in Sch A-I and Sch B suggest that the scheelite-fluid partition coefficient of Eu^{2+} may be greater than that of Eu^{3+}.

Acknowledgements

This study was funded by the Special Public Welfare Scientific Research fund Project by Ministry of Land and Resources, China (201511035), the National Natural Science Foundation of China (NSFC Grant 41502065), and CAS Creative and Interdisciplinary Program (Y433131A07). We would like to thank Xiaobo Zhang and Zeming Li for their help during field work. Rémy S. Poulin, Olga Plotinskaya, Shaoyong Jiang and an anonymous reviewer were acknowledged for their helpful comments.

References

Bell, K., Anglin, C.D., and Franklin, J.M. (1989) Sm-Nd and Rb-Sr isotope systematics of scheelites: Possible implications for the age and genesis of vein-hosted gold deposits. Geology, 17, 500–504.

Brugger, J., Lahaye, Y., Costa, S., Lambert, D., and Bateman, R. (2000) Inhomogeneous distribution of REE in scheelite and dynamics of Archaean hydrothermal systems (Mt. Charlotte and Drysdale gold deposits, Western Australia). Contributions to Mineralogy and Petrology, 139, 251–264.

Brugger, J., Maas, R., Lahaye, Y., McRae, C., Ghaderi, M., Costa, S., Lambert, D., Bateman, R., and Prince, K. (2002) Origins of Nd–Sr–Pb isotopic variations in single scheelite grains from Archaean gold deposits, Western Australia. Chemical Geology, 182, 203–225.

Brugger, J., Etschmann, B., Pownceby, M., Liu, W.H., Grundler, P., and Brewe, D. (2008). Oxidation state of europium in scheelite: Tracking fluid–rock interaction in gold deposits. Chemical Geology, 257, 26–33.

Burt, D.M. (1989) Compositional and phase relations among rare earth element minerals. Reviews in Mineralogy, 21, 259–307.

Catanzaro, E.J., Murphy, T.J., Garner, E.L., and Shields, W.R. (1966) Absolute isotopic abundance ratio and atomic weight of terrestrial rubidium. Journal of Research of the National Bureau of Standards, 73, 511–516.

Chang, Y.F., Liu, X.P., and Wu, Y.C. (1991) The copper-iron belt of the Lower and Middle Reaches of the Changjiang River. Beijing, Geological Publishing House, 379 p. (in Chinese with English abstract).

Chugaev, A.V., Chernyshov, I.V., Gamyanin, G.N., Bortnikov, N.S., and Baranova, A.N. (2010) Rb-Sr isotopic systematic of hydrothermal minerals, age, and matter sources of the Nezhdaninskoe gold deposit (Yakutia). Doklady Earth Sciences, 434, 1337–1341.

Darbyshire, D.P.F., Pitfield, P.E.J., and Campbell, S.D.G. (1996) Late Archean and Early Proterozoic gold-tungsten mineralization in the Zimbabwe Archean Craton: Rb-Sr and Sm-Nd isotope constraints. Geology, 24, 19–22.

Deditius, A.P., Reich, M., Simon, A.C., Suvorova, A., Knipping, J., Roberts, M.P., Rubanov, S.,

433 Dodd, A., and Saunders, M. (2018) Nanogeochemistry of hydrothermal magnetite.
434 Contributions to Mineralogy and Petrology, 173, https://doi.org/10.1007/s00410-018-1474-1n
435 Dostal, J., Kontak, D.J., and Chatterjee, A.K. (2009) Trace element geochemistry of scheelite and
436 rutile from metaturbidite-hosted quartz vein gold deposits, Meguma Terrane, Nova Scotia,
437 Canada: Genetic implications. Mineralogy and Petrology, 97, 95–109.
438 Elbaz-Poulichet, F., Seidel, J.L., Jézéquel, D., Metzger, E., Prévot, F., Simonucci, C., Szrazin, G.,
439 Viollier, E., Etcheber, H., Jouanneau, J.M., Weber, O., and Radakovitch, O. (2005).
440 Sedimentary record of redox-sensitive elements (U, Mn, Mo) in a transitory anoxic basin (the
441 Thau lagoon, France). Marine Chemistry, 95, 271–281.
442 Fu, Y., Sun, X., Zhou, H., Lin, H., Jiang, L., and Yang, T. (2017) In-situ LA-ICP-MS trace
443 elements analysis of scheelites from the giant Beiya gold–polymetallic deposit in Yunnan
444 Province, Southwest China and its metallogenic implications. Ore Geology Reviews, 80,
445 828–837.
446 Gaspar, M., Knaack, C., Meinert, L.D., and Moretti, R. (2008) REE in skarn systems: A
447 LA-ICP-MS study of garnets from the Crown Jewel gold deposit. Geochimica et
448 Cosmochimica Acta, 72, 185–205.Geisler, T., Schaltegger, U., and Tomaschek, F. (2007)
449 Re-equilibration of Zircon in Aqueous Fluids and Melts. Elements, 3, 43–50.
450 Geisler, T., Schaltegger, U., and Tomaschek, F., (2007) Re-equilibration of Zircon in Aqueous
451 Fluids and Melts. Elements, 3, 43–50.
452 Ghaderi, M., Palin, J.M., Campbell, I.H., and Sylvester, P.J. (1999) Rare earth element systematics
453 in scheelite from hydrothermal gold deposits in the Kalgoorlie-Norseman region, Western
454 Australia. Economic Geology, 94, 423–437.
455 Han, J.S., Chu, G.B., Chen, H.Y., Hollings, P., Sun, S.Q., and Chen, M. (2018) Hydrothermal
456 alteration and short wavelength infrared (SWIR) characteristics of the Tongshankou
457 porphyry-skarn Cu-Mo deposit, Yangtze craton, Eastern China. Ore Geology Reviews, 101,
458 143–164.
459 Hu, H., Lentz, D., Li, J.W., McCarron, T., Zhao, X.F., and Hall, D. (2014) Reequilibration
460 processes in magnetite from iron skarn deposits. Economic Geology, 110, 1–8.
461 Lai, J.Q., Chi, G.X., Peng, S.G., Shao, Y.J., and Yang, B. (2007) Fluid Evolution in the Formation
462 of the Fenghuangshan Cu-Fe-Au Deposit, Tongling, Anhui, China. Economic Geology, 102,

949−970.

Lei, X.F., Duan, D.F., Jiang, S.Y., and Xiong, S.F. (2018) Ore-forming fluids and isotopic (H-O-C-S-Pb) characteristics of the Fujiashan-Longjiaoshan skarn W-Cu-(Mo) deposit in the Edong District of Hubei Province, China. Ore Geology Reviews, 103, 386−405.

Li, J.W., Zhao, X.F., Zhou, M.F., Ma, C.Q., de Souza, Z.S., and Vasconcelos, P. (2009) Late Mesozoic magmatism from the Daye region, eastern China: U–Pb ages, petrogenesis, and geodynamic implications. Contributions to Mineralogy and Petrology, 157, 383–409.

Li, J.W., Zhao, X.F., Zhou, M.F., Vasconcelos, P., Ma, C.Q., Deng, X.D., Sérgio de Souza, Z., Zhao, Y.X., and Wu, G. (2008) Origin of the Tongshankou porphyry–skarn Cu–Mo deposit, eastern Yangtze craton, Eastern China: geochronological, geochemical, and Sr–Nd–Hf isotopic constraints. Mineralium Deposita, 43, 315–336.

Li, X.H., Li, W.X., Wang, X.C., Li, Q.L., Liu, Y., Tang, G.Q., Gao, Y.Y., and Wu, F.Y. (2010) SIMS U–Pb zircon geochronology of porphyry Cu–Au–(Mo) deposits in the Yangtze River Metallogenic Belt, eastern China: magmatic response to early Cretaceous lithospheric extension. Lithos, 119, 427–438.

Ling, M.X., Wang, F.Y., Ding, X., Hu, Y.H., Zhou, J.B., Zartman, R.E., Yang, X.Y., and Sun, W.D. (2009) Cretaceous ridge subduction along the lower Yangtze River belt, eastern China. Economic Geology, 104, 303–321.

Lipin, B.R., and McKay, G.A. (1989) Geochemistry and mineralogy of rare earth elements. Mineralogical Society of America, Reviews in Mineralogy, 21, 169–200.

Liu, Y., Hu, Z., Gao, S., Günther, D., Xu, J., Gao, C., and Chen, H. (2008) In situ analysis of major and trace elements of anhydrous minerals by LA-ICP-MS without applying an internal standard. Chemical Geology, 257, 34–43.

Lv, X.B., Yao, S.Z., and Lin, X.D. (1992) The geological characteristics and ore-forming mechanism of Tongshankou skarn-porphyry composite type of copper (molybdenum) ore deposit, Hubei. Earth Science-Journal of China University of Geosciences, 17, 171–180 (in Chinese with English abstract).

Nassau, K., Loiacono, G.M. (1963) Calcium tungstate-III: trivalent rare earth substitution. Journal of Physics and Chemistry of Solids, 24, 1503–1510.

Noble, S.R., Spooner, E.T.C., and Harris, F.R. (1984) The Logtung large tonnage, low-grade W

(scheelite)-Mo porphyry deposit, south-central Yukon Territory. Economic Geology, 79, 848–868.

Plotinskaya. O.Y., Baksheev I.A., and Minervina, E.A. (2018) REE distribution in scheelite from the Yubileinoe porphyry gold deposit, South Urals: evidence from LA-ICP-MS data. Geology of Ore Deposits, 60, 355–364.

Poulin, R.S., Kontak, D.J., McDonald, A., and McCLenaghan M.B. (2018) Assessing scheelite as an ore-deposit discriminator using its trace-element and REE chemistry. The Canadian Mineralogist, 56, 265–302.

Putnis, A. (2002) Mineral replacement reactions: From macroscopic observations to microscopic mechanisms. Mineralogical Magazine, 66, 689–708.

Putnis, A. (2009) Mineral Replacement Reactions. Reviews in Mineralogy and Geochemistry, 70, 87–124.

Rusk, B.G., Reed, M.H. (2002) Scanning electron microscope–cathodoluminescence analysis of quartz reveals complex growth histories in veins from the Butte porphyry copper deposit, Montana. Geology, 30, 727–730.

Rusk, B.G., Lowers, H.A., Reed, M.H. (2008) Trace elements in hydrothermal quartz: Relationships to cathodoluminescent textures and insights into vein formation. Geology, 36, 547–550.

Scanlan E.J., Scott J.M., Wilson V.J., Stirling C.H., Reid M.R. and Le Roux P.J. (2018) In Situ $^{87}Sr/^{86}Sr$ of Scheelite and Calcite Reveals Proximal and Distal Fluid-Rock Interaction During Orogenic W-Au Mineralization, Otago Schist, New Zealand. Economic Geology, 113, 1571–1586.

Shen, J., Qin, L., Fang, Z., Zhang, Y., Liu, J., Liu, W., Wang, F., Xiao, Y., Yu, H., and Wei, S. (2018) High-temperature inter-mineral Cr isotope fractionation: A comparison of ionic model predictions and experimental investigations of mantle xenoliths from the North China Craton. Earth and Planetary Science Letters, 499, 278-290.

Shu, Q.A., Chen, P.R., and Chen, J.R. (1992) Geology of Fe–Cu Ore Deposits in Eastern Hubei Province. Press of Metallurgical Industry, Beijing, p 532 (in Chinese with English abstract).

Smith, M.P., Henderson, P., Jeffries, T. E. R., Long, J., and Williams, C.T. (2004) The rare earth elements and uranium in garnets from the Beinn an Dubhaich aureole, Skye, Scotland, UK:

Constraints on processes in a dynamic hydrothermal system. Journal of Petrology, 45, 457–484.

Song, G.X., Qin, K.Z., Guangming, L.I., Evans, N.J., and Chen, L. (2014) Scheelite elemental and isotopic signatures:Implications for the genesis of skarn-type W-Mo deposits in the Chizhou Area,Anhui Province,Eastern China. American Mineralogist, 99, 303–317.

Sun, K.K., and Chen, B. (2017) Trace elements and Sr-Nd isotopes of scheelite: Implications for the W-Cu-Mo polymetallic mineralization of the Shimensi deposit, South China. American Mineralogist, 102, 1114–1128.

Uspensky, E., Brugger, J., and Gräser, S. (1998) REE geochemistry systematics of scheelite from the Alps using luminescence spectroscopy: From global regularities to facies control. Schweizerische Mineralogische und Petrographische Mitteilungen, 78, 33–56.

Wang, Q., Zhao, Z.H., Bao, Z.W., Xu, J.F., Liu, W., Li, C.F., Bai, Z.H., and Xiong, X.L. (2004) Geochemistry and Petrogenesis of the Tongshankou and Yinzu Adakitic Intrusive Rocks and the Associated Porphyry Copper-Molybdenum Mineralization in Southeast Hubei, East China. Resource Geology, 54, 137–152.

Ware, B.D., Jourdan, F., Merle, R., Chiaradia, M., and Hodges, K., (2018) The Kalkarindji Large Igneous Province, Australia: Petrogenesis of the Oldest and Most Compositionally Homogenous Province of the Phanerozoic. Journal of Petrology, 59, 635–665.

Whitney, D.L., and Evans, B.W., (2010) Abbreviations for names of rock-forming minerals. American Mineralogist, 95, 185–187.

Wood, S.A., and Samson, I.M. (2000) The hydrothermal geochemistry of tungsten in granitoid environments: I. Relative solubilities of ferberite and scheelite as a function of T, P, pH, and m_{NaCl}. Economic Geology, 95, 143–182.

Xia, J.L., Huang, G.C., Ding, L.X., and Cheng, S.B. (2015) In Situ Analyses of Trace Elements, U–Pb and Lu–Hf Isotopes in Zircons from the Tongshankou Granodiorite Porphyry in Southeast Hubei Province, Middle-Lower Yangtze River Metallogenic Belt, China. Acta Geologica Sinica (English Edition), 89, 1588–1600.

Xie, G.Q., Mao, J.W., Li, W., Zhu, Q.Q., Liu, H.B., Jia, G.H., Li, Y.H., Li, J.J., and Zhang, J. (2016) Different proportion of mantle-derived noble gases in the Cu–Fe and Fe skarn deposits:

552 He–Ar isotopic constraint in the Edong district, Eastern China. Ore Geology Reviews, 72,
553 343–354.
554 Xie, G.Q., Mao, J.W., Zhao, H.J., Duan, C., and Yao, L. (2012) Zircon U–Pb and phlogopite
555 ^{40}Ar–^{39}Ar age of the Chengchao and Jinshandian skarn Fe deposits, southeast Hubei Province,
556 Middle–Lower Yangtze River Valley metallogenic belt, China. Mineralium Deposita, 47,
557 633–652.
558 Xie, G.Q., Mao, J.W., Zhu, Q.Q., Yao, L., Li, Y.H., Li, W., and Zhao, H.J. (2015) Geochemical
559 constraints on Cu–Fe and Fe skarn deposits in the Edong district, Middle–Lower Yangtze
560 River metallogenic belt, China. Ore Geology Reviews, 64, 425–444.
561 Xu, Y.M., and Jiang, S.Y. (2017) In-situ analysis of trace elements and Sr-Pb isotopes of
562 K-feldspars from Tongshankou Cu-Mo deposit, SE Hubei Province, China: Insights into early
563 potassic alteration of the porphyry mineralization system. Terra Nova, 29, 343–355.
564 Zeng, L.P., Zhao, X.F., Li, X.C., Hu, H., and McFarlane, C. (2016) In situ elemental and isotopic
565 analysis of fluorapatite from the Taocun magnetite-apatite deposit, Eastern China: Constraints
566 on fluid metasomatism. American Mineralogist, 101, 2468–2483.
567 Zhang, L., Ren, Z.Y., Nichols, A.R.L., Zhang, Y.H., Zhang, Y., Qian, S.P., and Liu, J.Q. (2014)
568 Lead isotope analysis of melt inclusions by LA-MC-ICP-MS. Journal of Analytical Atomic
569 Spectrometry, 29, 1393–1405.
570 Zhang, L., Ren, Z.Y., Wu, Y.D., and Li, N. (2018) Sr isotope measurement of basaltic glasses by
571 LA-MC-ICP-MS based on a linear relationship between analytical bias and Rb/Sr ratios.
572 Rapid Communications in Mass Spectrometry, DOI: 10.1002/rcm.8011.
573 Zhao, J., Brugger, J., Ngothai, Y., and Pring, A. (2014) The replacement of chalcopyrite by bornite
574 under hydrothermal conditions. American Mineralogist, 99, 2389–2397.
575 Zhao, W.W., Zhou, M.F., Williams-Jones, A.E., and Zhao, Z. (2018) Constraints on the uptake of
576 REE by scheelite in the Baoshan tungsten skarn deposit, South China. Chemical Geology,
577 477, 123–136.
578 Zhou, T.F., Wang, S.W., Fan, Y., Yuan, F., Zhang, D.Y., and White, N.C. (2015) A review of the
579 intracontinental porphyry deposits in the Middle-Lower Yangtze River Valley metallogenic
580 belt, Eastern China. Ore Geology Reviews, 65, 433–456.
581 Zhu, Z.Y., Jiang, S.Y., Hu, J., Gu, L.X., and Li, J. (2014). Geochronology, geochemistry, and

582 mineralization of the granodiorite porphyry hosting the Matou Cu–Mo (±W) deposit, Lower
583 Yangtze River metallogenic belt, eastern China. Journal of Asian Earth Sciences, 79,
584 623–640.
585 Zhu, Q.Q., Xie, G.Q., and Han, Y.X. (2018) Characteristics of tungsten mineralization from the
586 Tongshankou skarn-porphyry Cu (Mo) deposit in Daye, Hubei province, and its geological
587 implications. Earth Science, doi: 10.3799/dqkx.2018.288

588 **Figure captions**

589 **Fig. 1** a) Geological map of magmatic rocks and deposits in the Middle-Lower
590 Yangtze River Valley Metallogenic Belt (modified from Chang et al., 1991). TLF:
591 Tancheng-Lujiang fault, XGF: Xiangfan-Guangji fault, YCF: Yangxing-Changzhou
592 fault; b) Geological map of the Edong district, showing mineralization types and their
593 emplacement age (modified from Xie et al., 2012). Different sizes of circles indicate
594 the size of the deposit. Sample dating locations are from (Li et al., 2008, 2009; Xie et
595 al., 2012).

596 **Fig. 2** Cross section of the No. 8 prospecting line.

597 **Fig. 3** Photographs and photomicrographs of samples from the Tongshankou deposit.
598 a) Mafic enclave contained in the granodiorite porphyry; b) Hand sample of altered
599 granodiorite porphyry. Sulfides such as pyrite and bornite could be observed; c) Hand
600 sample of altered granodiorite porphyry under ultraviolet light. Disseminated scheelite
601 could be observed distributing in the granodiorite porphyry; d) Hand sample of skarn.
602 Brown garnet could be observed with retrograde alteration minerals distributing in the
603 sides of garnet; e) Hand sample of skarn under ultraviolet light. Scheelite could be
604 observed coexisting with retrograde alteration minerals; f) Hand sample of distal
605 marble, with quartz-sulfide vein crosscutting it; g) Hand sample of distal marble
606 under ultraviolet light. Scheelite could be observed distributing in the quartz veins.
607 Abbreviations from Whitney and Evans (2010) Ccp: Chalcopyrite; Py: Pyrite; Qz:
608 Quartz; Bn: Bornite; Grt: Garnet.

609 **Fig. 4** Photomicrographs of scheelite occurrences in the Tongshankou deposit. a) and
610 c) Scheelite in the altered granodiorite porphyry (Sch A), coexisting with calcite.

Plane-polarized photomicrograph; b) and d) Cathodoluminescence (CL) image of Sch A. The blue luminescence of Sch A-I is vaguely zoned. The Sch-II shows lighter blue luminescence and a concentration of blue-white luminescent veins. Many veins are seen to traverse Sch A-I; e) Scheelite in the skarn (Sch B), coexisting with sericite. Cross-polarized photomicrograph; f) CL image of Sch B; g) Scheelite in the distal marble contained in the quartz vein (Sch C). Plane-polarized photomicrograph; h) CL image of Sch C. Cal: Calcite; Ser: Sericite; Qz: Quartz; Ccp: Chalcopyrite.

Fig. 5 Chondrite-normalized REE patterns of scheelite from the Tongshankou deposit and SEM-CL images of represented scheelite. a) Sch A show complex REE patterns, with Sch A-I displaying negative Eu anomalies and HREE depletions while Sch A-II displaying positive Eu anomalies and elevated HREE; b) Complex textures of Sch A could be observed. I: Cl-bright gray, mostly concentrically-zoned scheelite; II: CL-dark gray, complexly zoned scheelite. A close-up of a pore is shown on the upper right corner, showing the existence of mica based on the cleavage in the pore; c) Sch B exhibit exclusively positive Eu anomalies and steep HREE depletion; d) Rhythmically zoned, broadly homogeneous CL character of Sch B; e) Sch C show HREE depletion and primarily small negative Eu anomalies; f) Rhythmically zoned, broadly homogeneous CL appearance of Sch C.

Fig. 6 a) Plot of Eu/Eu* vs. Sr concentration of scheelite; b) Plot of Eu/Eu* vs. Mo concentration of scheelite

Fig. 7 In situ Sr isotopes for scheelite and calcites compared with whole-rock Sr isotopes of the granodiorite porphyries and mafic enclaves in the Tongshankou

deposit. GP: granodiorite porphyries; ME: mafic enclaves.

Fig. 8 a) Plot of Nb+Ta vs. ∑REE-Eu+Y of scheelite; b) Plot of Na vs. ∑REE-Eu+Y of scheelite.

Fig. 9 a) Metallogenic model for the Tongshankou primary Cu-W deposits. b) The dissolution-reprecipitation process of Sch A into Sch A-I and Sch A-II.

This is a preprint, the final version is subject to change, of the American Mineralogist (MSA)
Cite as Authors (Year) Title. American Mineralogist, in press.
DOI: https://doi.org/10.2138/am-2020-7194

Figure 1a

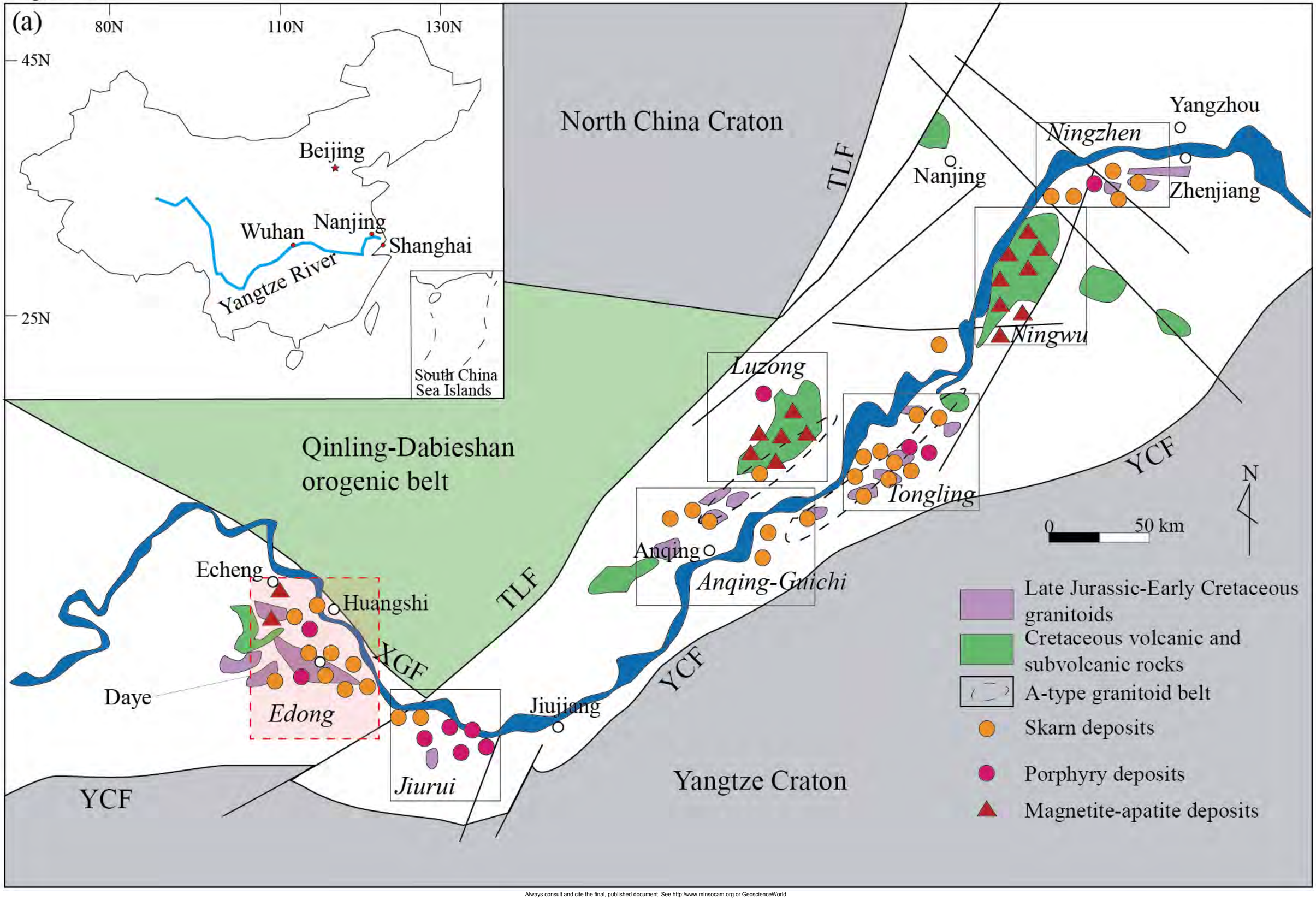

This is a preprint, the final version is subject to change, of the American Mineralogist (MSA)
Cite as Authors (Year) Title. American Mineralogist, in press.
DOI: https://doi.org/10.2138/am-2020-7194

Figure 1b

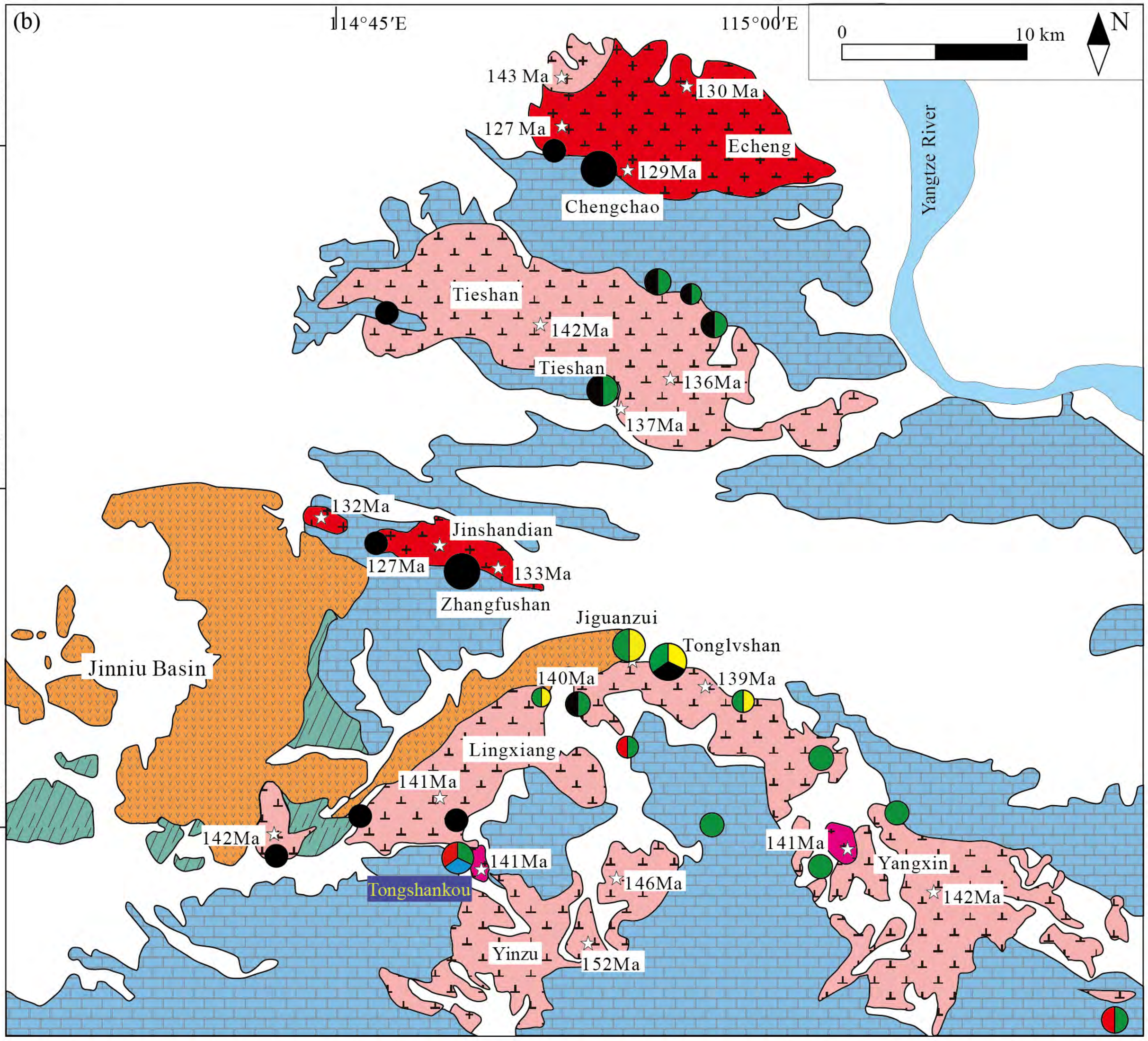

This is a preprint, the final version is subject to change, of the American Mineralogist (MSA)
Cite as Authors (Year) Title. American Mineralogist, in press.
DOI: https://doi.org/10.2138/am-2020-7194

Figure 2

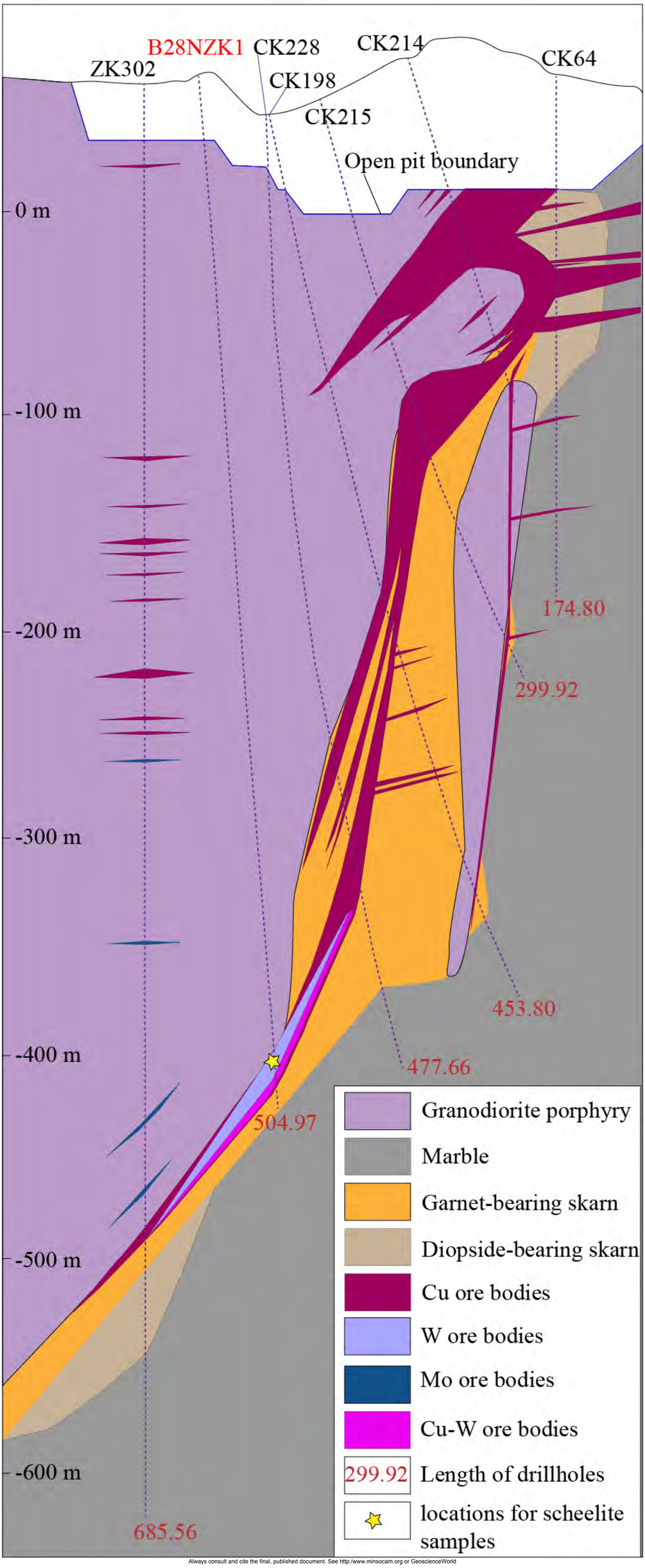

This is a preprint, the final version is subject to change, of the American Mineralogist (MSA)
Cite as Authors (Year) Title. American Mineralogist, in press.
DOI: https://doi.org/10.2138/am-2020-7194

Figure 3

This is a preprint, the final version is subject to change, of the American Mineralogist (MSA)
Cite as Authors (Year) Title. American Mineralogist, in press.
DOI: https://doi.org/10.2138/am-2020-7194

Fig. 4

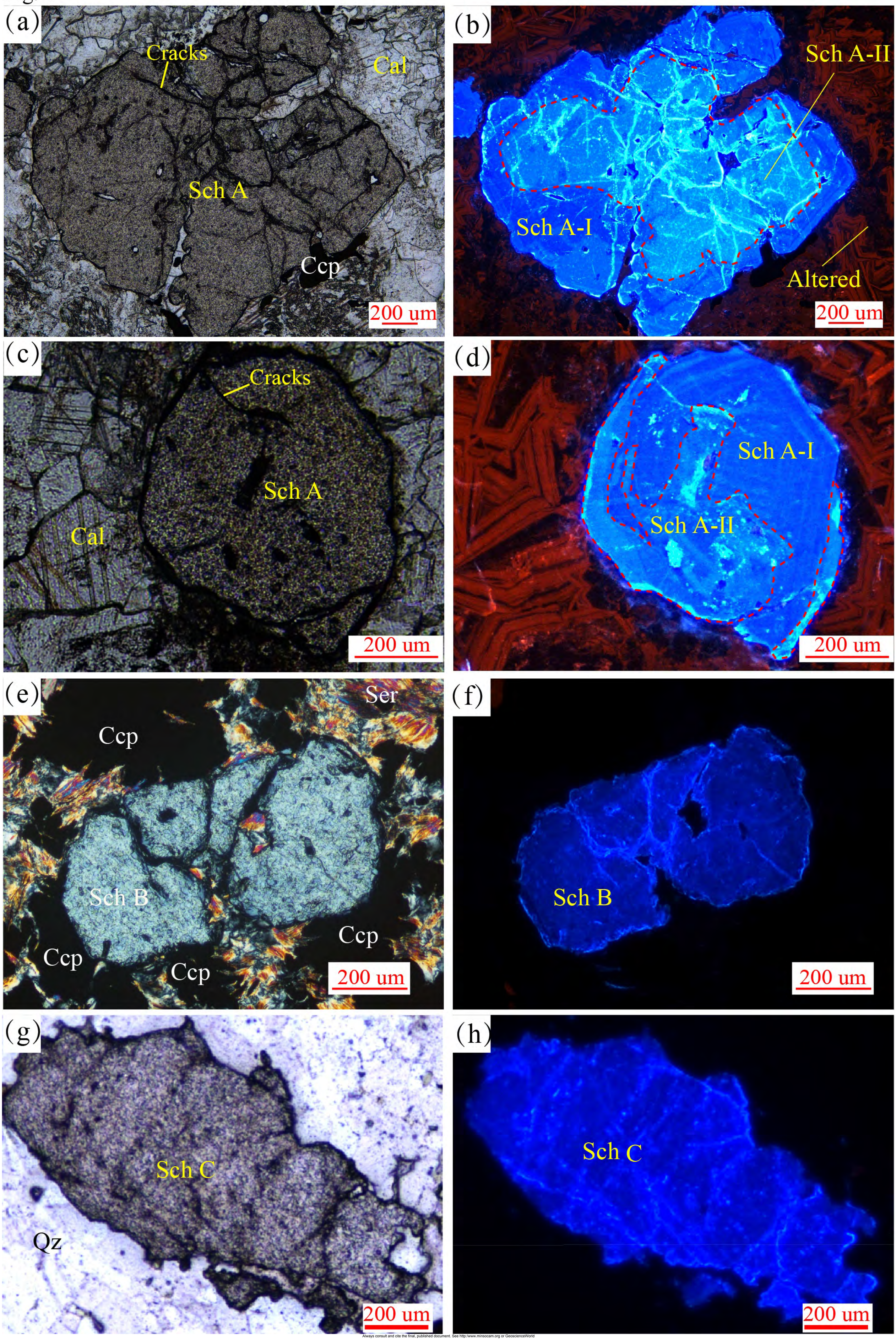

This is a preprint, the final version is subject to change, of the American Mineralogist (MSA)
Cite as Authors (Year) Title. American Mineralogist, in press.
DOI: https://doi.org/10.2138/am-2020-7194

Figure 5

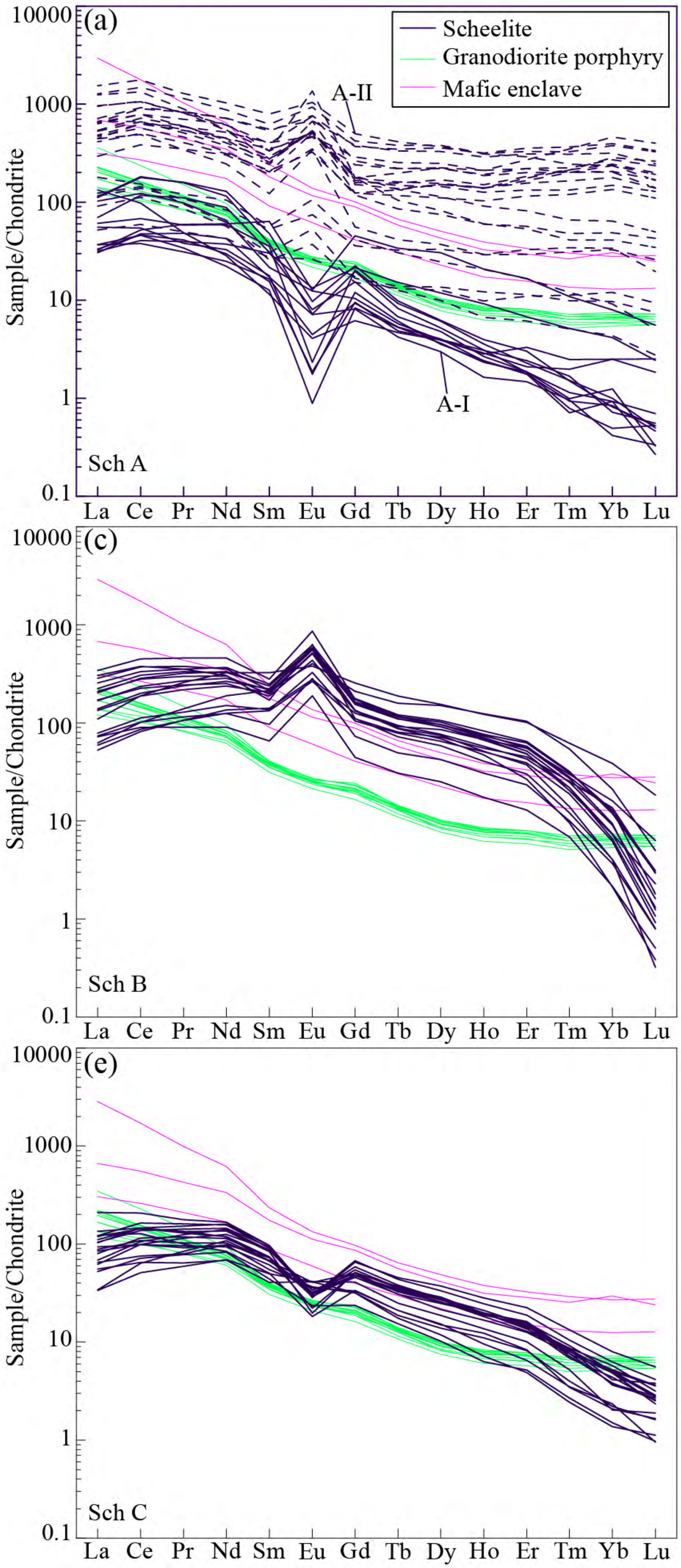

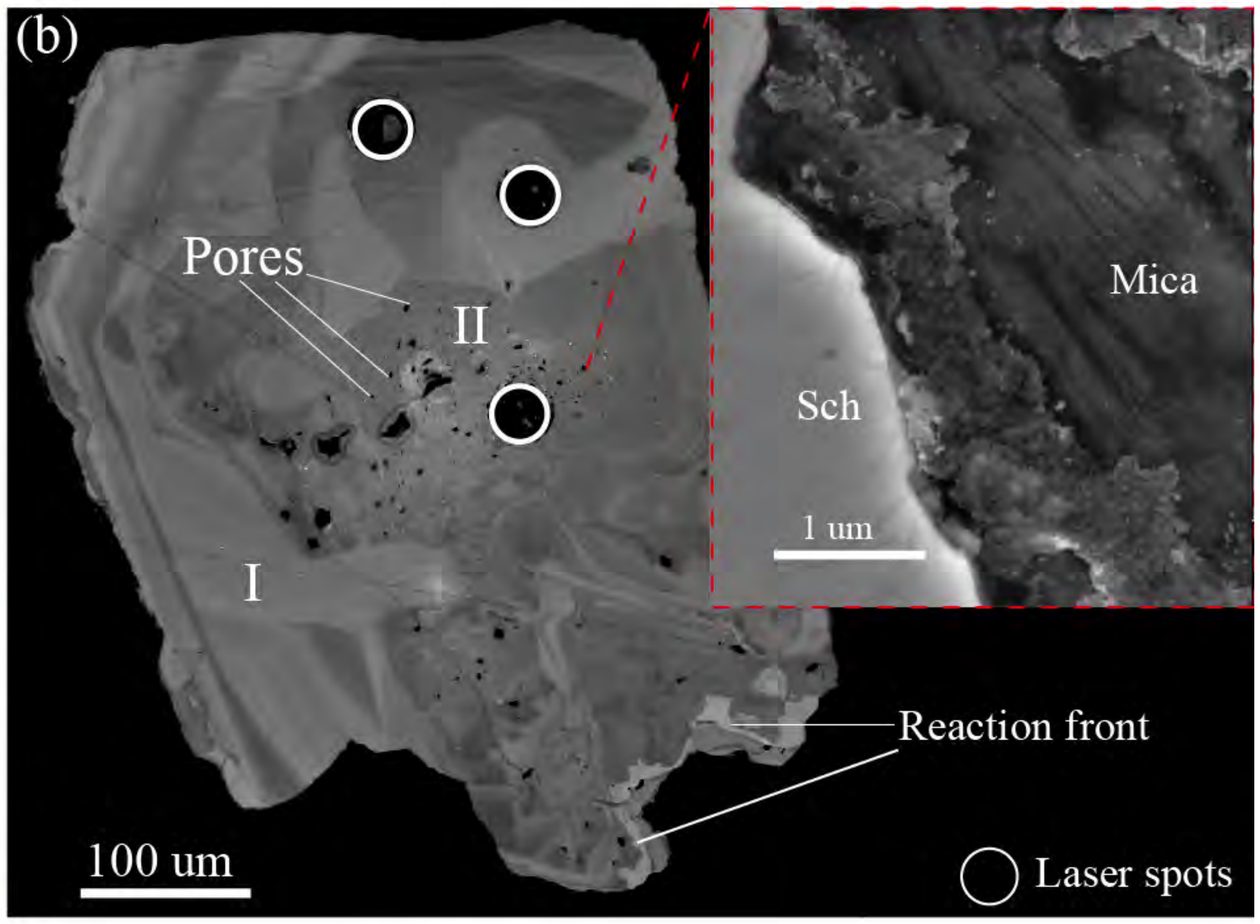

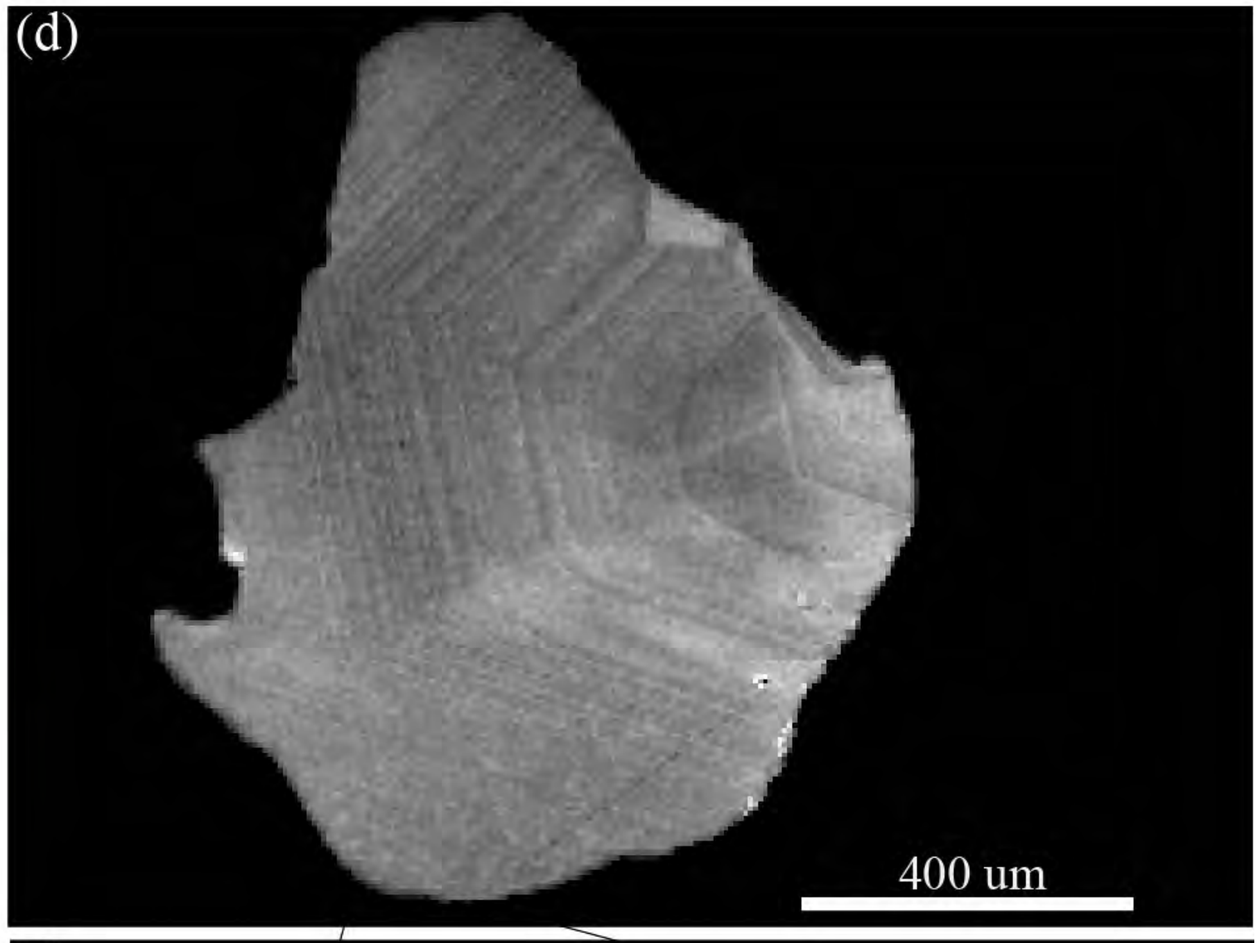

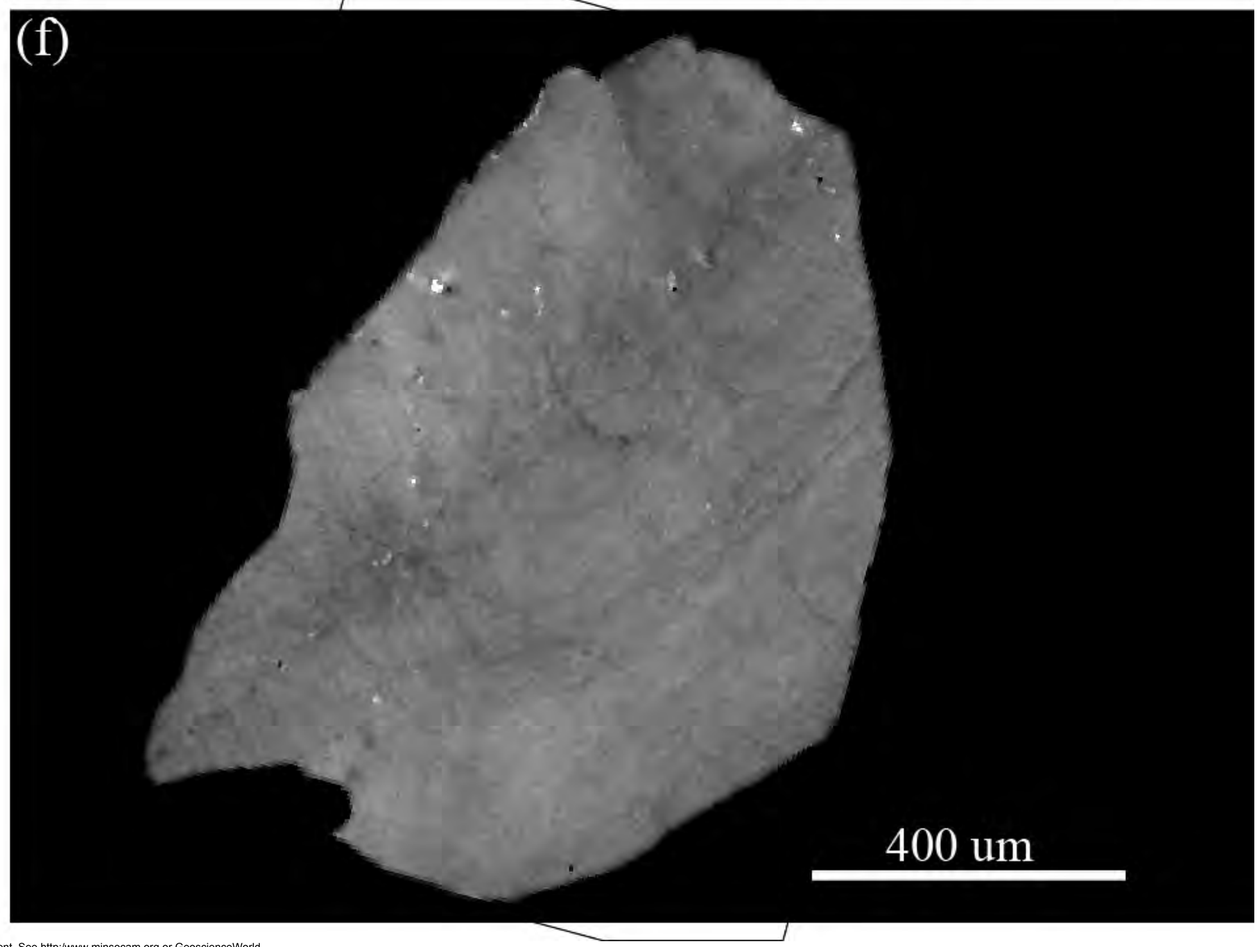

This is a preprint, the final version is subject to change, of the American Mineralogist (MSA)
Cite as Authors (Year) Title. American Mineralogist, in press.
DOI: https://doi.org/10.2138/am-2020-7194

Fig. 6

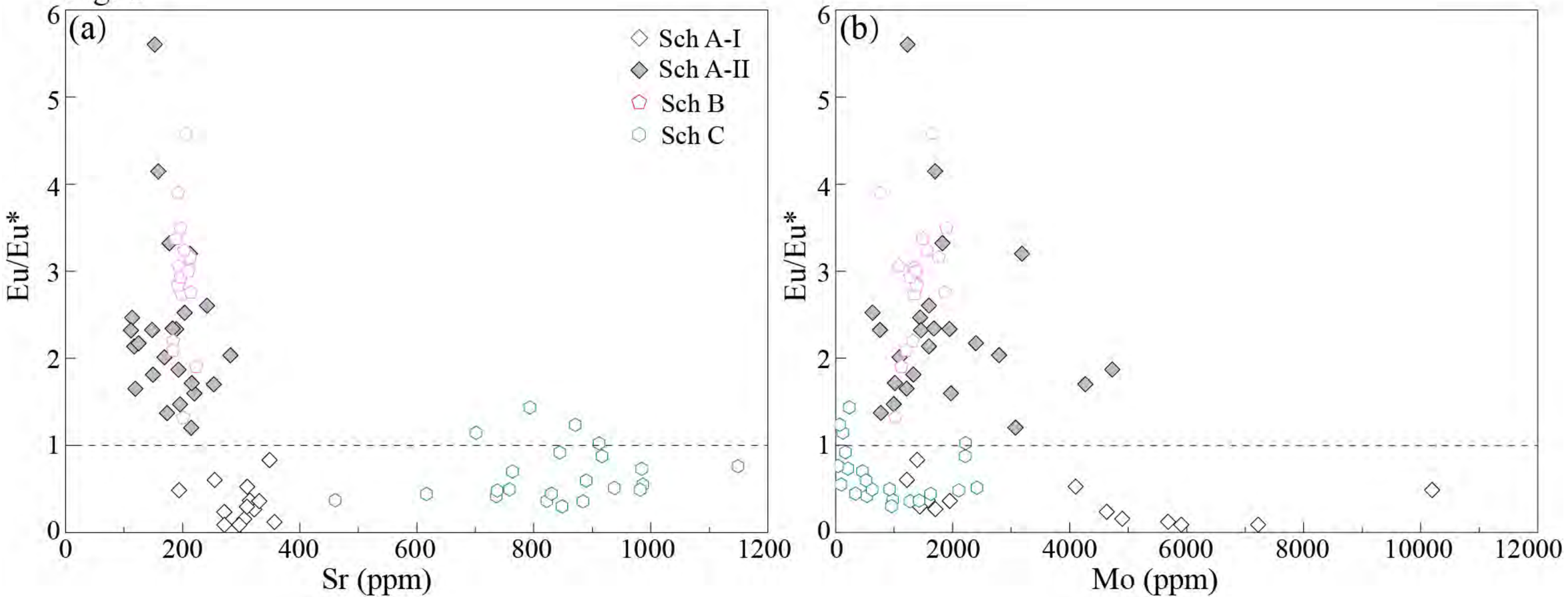

Figure 7

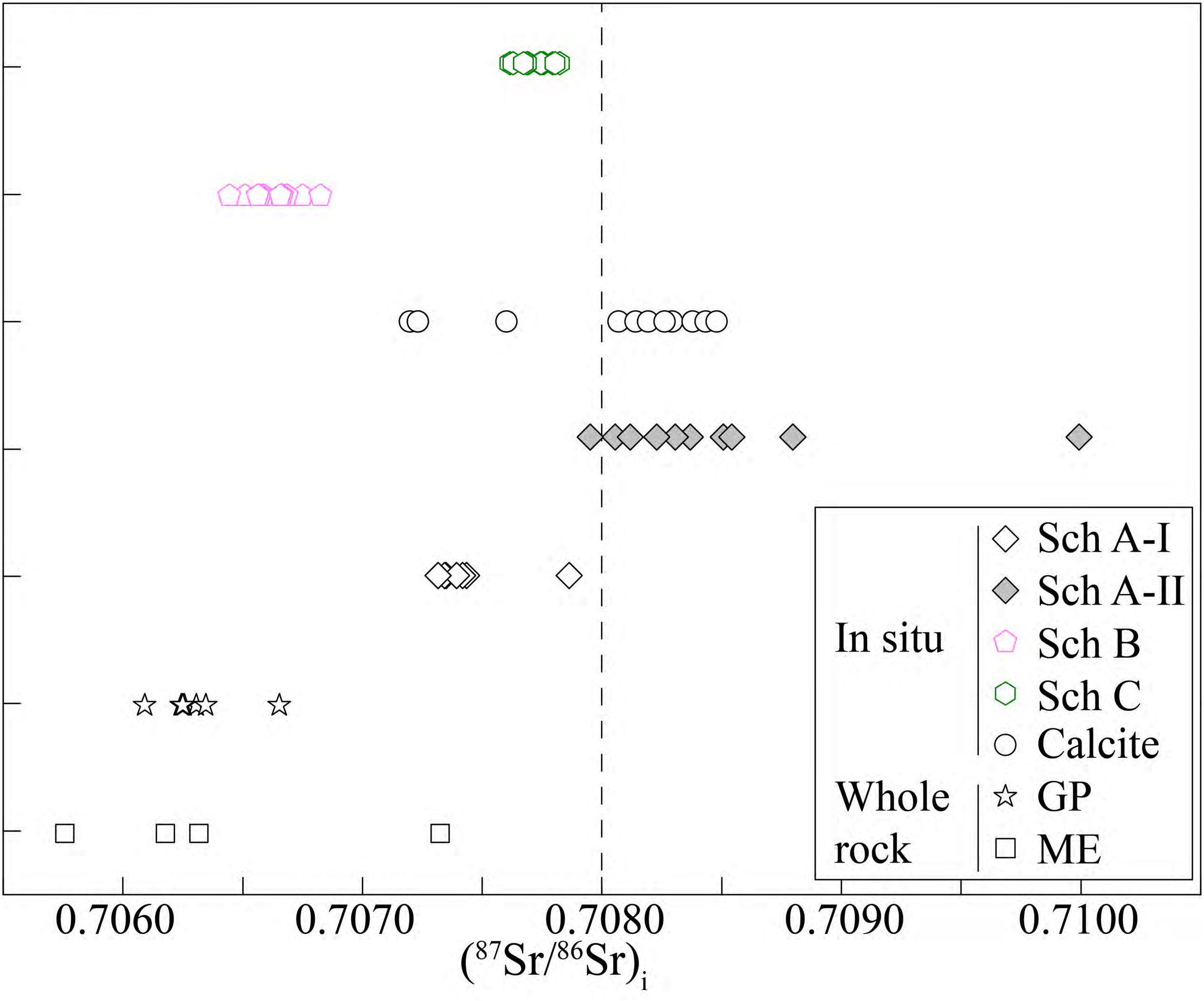

Fig. 8

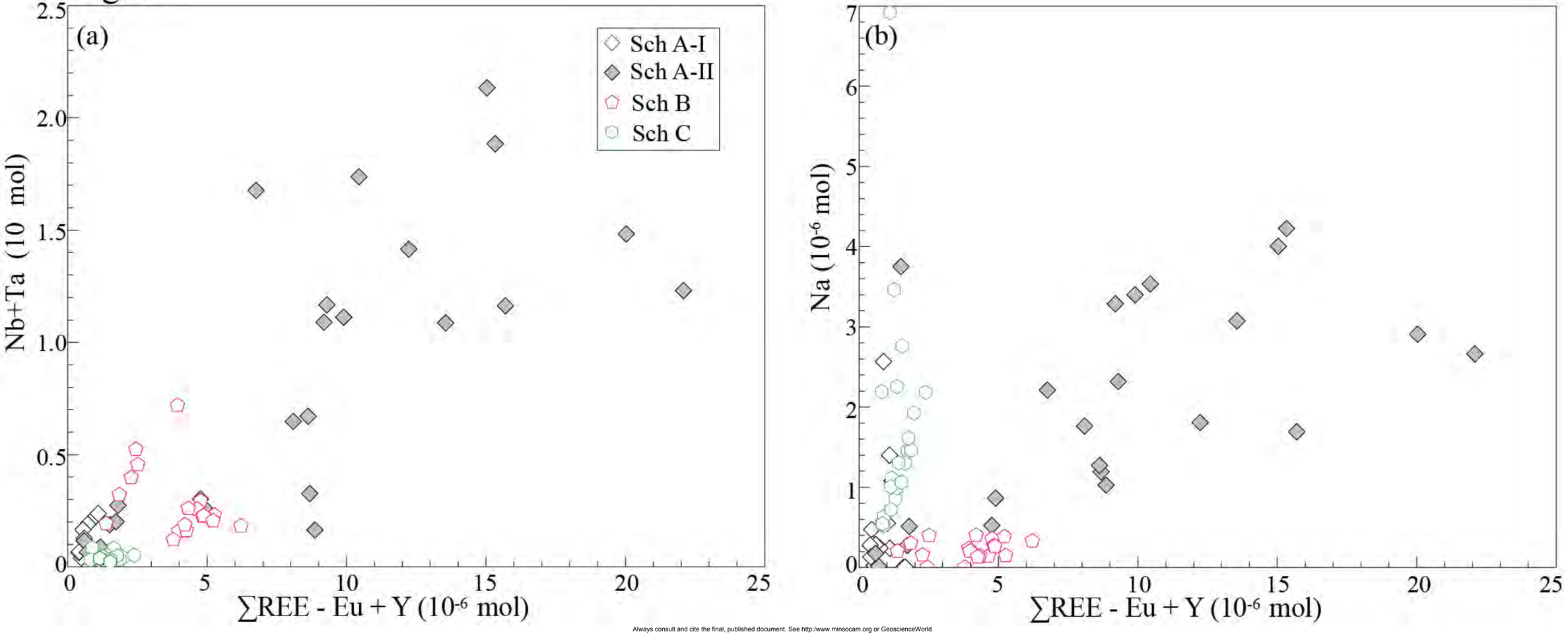

This is a preprint, the final version is subject to change, of the American Mineralogist (MSA)
Cite as Authors (Year) Title. American Mineralogist, in press.
DOI: https://doi.org/10.2138/am-2020-7194

Fig. 9